ingegneria sismica
International Journal of Earthquake Engineering
Anno XLIII - Num. 1 - 2026

Research on power line coordinate domain model based on wireless localization of IOT (gim-rtk)

Junjie Sun[1,*], *Xiang Yuan*[1], *Keji Chen*[1], *Bing Wu*[1], *Jiarui Yang*[1] *and Chutian Yu*[1]

[1] Economic and Technological Research Institute of State Grid Zhejiang Electric Power Co., Ltd. Hangzhou, Zhejiang, 310000 China

SUMMARY: *How to accurately and rapidly obtain target point coordinate information within large-scale, topographically complex power line networks is a common concern for power construction, inspection, and surveying operations. This paper proposes four coordinate unification techniques based on the irregularity of radio wave propagation: calibrated coordinate transformation, hand-eye calibration, feature matching, and world coordinate systems. Simultaneously, it employs compressed sensing theory to solve the direction of arrival (DOA) estimation for wireless positioning coordinates, incorporating a distance metric function to enhance estimation accuracy. The DOA estimation problem is transformed into a sparse signal reconstruction problem, utilizing an iterative shrinkage (parallel coordinate descent) algorithm to perform scalar shrinkage on the provisional coordinate direction solution. This establishes a parallel coordinate descent-based wireless positioning direction estimation method. After achieving coordinate unification and direction estimation for target points, particle filtering technology and w-KNN matching algorithms are integrated. RTK technology is employed to obtain the three-dimensional coordinates of target points, forming a power line coordinate domain model. In simulation experiments, the proposed wireless positioning direction estimation algorithm maintains relative error within [0.00, 1.00]%, demonstrating both computational accuracy and robustness.*

KEYWORDS: *Coordinate Unification; Parallel Coordinate Descent; Power Line Coordinate Domain; Wireless Positioning Direction Estimation; RTK*

1 Introduction

The safe and reliable operation of transmission lines depends to a significant extent on the health status of their equipment components. However, due to variations in material composition and operating environments, the service life and degree of aging of these components differ considerably [1, 2]. Consequently, the comprehensive health status of all line equipment components becomes a critical indicator for assessing the overall health of the transmission line. This indicator is derived from our data management of power lines, achieved through detection, inspection, and analysis to enable effective operation and maintenance [3-5]. Currently, power line data management primarily relies on periodic and ad hoc inspections and examinations. Patrol personnel record the results of these activities, which are subsequently compiled and analyzed to determine the operational status of equipment and components [6-8]. However, since most of these management tasks are phased and cyclical, coupled with non-standardized data collection methods and field personnel recording practices, the data

*sjj0518288@163.com
https://doi.org/10.65102/is2026259
Published: 30 April, 2026

commonly suffers from issues such as poor continuity, timeliness, accuracy, and validity, thereby diminishing its practical value [9-12].

Real-Time Kinematic (RTK) measurement systems integrate GPS surveying technology with data transmission technology, representing a new breakthrough in GPS surveying [13, 14]. RTK measurement technology is a real-time differential GPS technique based on carrier phase observations. Gim-RTK wireless positioning integrates IoT wireless transmission capabilities to synchronize RTK positioning data in real time with power management systems, forming a dynamic coordinate domain. This enables efficient power facility data management through precise positioning [15-18].

This paper elucidates the irregularity of radio wave propagation by analyzing mathematical definition formulas and planar projection characteristics. Building upon this theoretical foundation, it sequentially describes four coordinate unification methods: calibration-based coordinate transformation, hand-eye calibration, feature matching, and world coordinate system unification. Subsequently, a DOA estimation model based on compressed sensing is introduced, outlining its operational steps and existing limitations to establish a wireless positioning direction estimation method for power line target points. Performance comparison experiments are then designed to select optimal filtering techniques and classification algorithms. After confirming the feasibility of the proposed wireless positioning direction estimation technology through simulation experiments, an RTK-based coordinate domain model for power lines is constructed, and its positioning accuracy performance is verified.

2 Coordinate Unification Technology Based on Radio Propagation

2.1 Irregularities in Radio Propagation

The simplified RSS model assumes that the communication coverage of an omnidirectional antenna is circular. In reality, due to factors such as the environment and the device itself, the coverage of any omnidirectional antenna is not a standard circle. This characteristic can be described by radio propagation irregularity. Radio propagation irregularities in Line-of-Sight (LoS) environments are primarily caused by the heterogeneity of the propagation medium and the devices. The Radio Irregularity Model (RIM) for WSN nodes is shown in Equation (1). Note that for clarity of presentation, angle values in this chapter omit the degree symbol.

$$G_\lambda(\hat{d}) = G_\lambda\left(d_0\right) - 10K_\lambda \eta \lg\left(\frac{\hat{d}}{d_0}\right) + F_{\sigma,\lambda} \tag{1}$$

Here, $G_\lambda(\hat{d})$ denotes the received signal strength at distance $\hat{d}$ in the direction of angle λ, d_0 is the reference distance, η represents path loss, and $F_{\sigma,\lambda}$ is Gaussian noise with standard deviation σ in the direction of angle λ. K_λ is the irregularity coefficient in the direction of angle λ, as shown in Equation (2).

$$K_\lambda = \begin{cases} 1, & \lambda = 0 \\ K_{\lambda-1} \pm \mathrm{Rand}_{\alpha,\beta}\, DOI, & \lambda \in (0,360) \bigcap \mathbb{N} \\ & s.t. \left|K_0 - K_{359}\right| \le DOI \end{cases} \tag{2}$$

$\text{Rand}_{\alpha,\beta}$ is a Weibull random variable with shape parameter α and scale parameter β. $\text{DOI} > 0$ represents radio propagation irregularity, whose values depend on the communication environment and hardware equipment. α, β, and DOI can be obtained experimentally or using empirical values. $\mathbb{N}$ denotes the set of natural numbers. When λ is not an integer, K_λ is computed as the difference between $K_{\lfloor\lambda\rfloor}$ and $K_{\lceil\lambda\rceil}$, as shown in Equation (3), where $\lambda \in (0, 360)$.

$$K_\lambda = K_{\lfloor\lambda\rfloor} + (\lambda - \lfloor\lambda\rfloor)\left(K_{\lceil\lambda\rceil} - K_{\lfloor\lambda\rfloor}\right) \tag{3}$$

The projections of the radio propagation irregularity model onto a two-dimensional plane are shown in Figures 1–3, where $\alpha = 0.67, \beta = 0.16, \hat{d} = 1\text{m}$. It can be observed that as DOI increases, the radio propagation irregularities become increasingly pronounced.

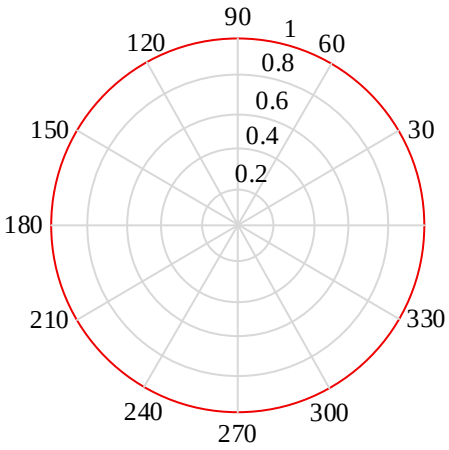

Figure 1: $DOI = 0$

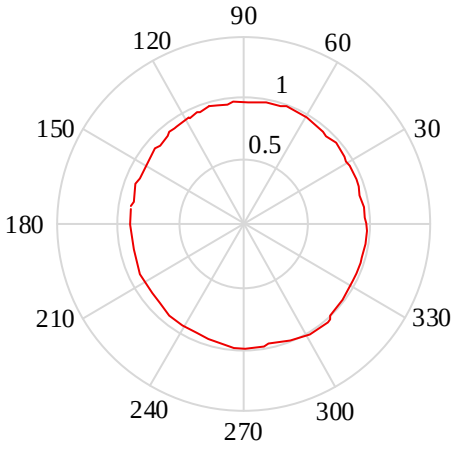

Figure 2: $DOI = 0.015$

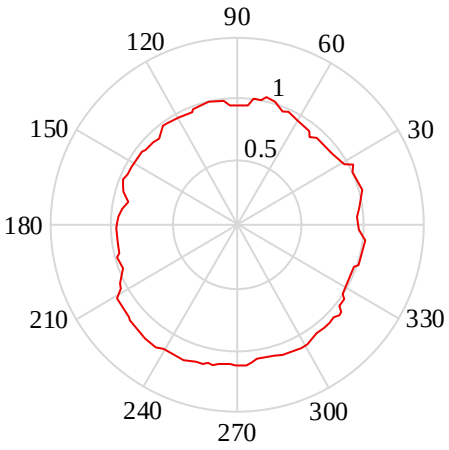

Figure 3: $DOI = 0.03$

Since sensor networks represent a special form of self-organizing networks, the radio propagation irregularity model in Equation (1) is also applicable to other mobile self-organizing networks. According to Equation (2), the difference in irregularity coefficients along the $\overrightarrow{\mathbf{AB}}$ and $\overrightarrow{\mathbf{AM}}$ directions in Figure 1 should fall within a reasonable range. LVS-RI precisely leverages this principle derived from the radio propagation irregularity model to verify node positions (detecting SDM attacks).

2.2 Coordinate Unification Techniques

In the integrated design of Bluetooth AOA positioning systems and visual positioning systems, coordinate unification serves as the critical step for converting the output data from both systems into a unified coordinate system. Specific methods for coordinate unification include calibration-based coordinate transformation, hand-eye calibration, feature matching, and world coordinate system unification.

2.2.1 Calibration-Based Coordinate Transformation Method

The principle involves determining the transformation relationship between the Bluetooth AOA coordinate system and the visual coordinate system (rotation matrix R and translation vector t) through calibration experiments, then converting Bluetooth AOA data into the visual coordinate system. The specific process is as follows:

(1) Place multiple calibration points with known positions within the target area. Record their coordinates in both the Bluetooth AOA coordinate system and the visual coordinate system. Let the coordinates of a calibration point in the Bluetooth AOA coordinate system be $P_{aoa} = \left[x_{aoa}, y_{aoa}, z_{aoa}\right]^T$ and their coordinates in the visual coordinate system as $P_{vis} = \left[x_{vis}, y_{vis}, z_{vis}\right]^T$.

(2) Calculate the rotation matrix R and translation vector t using least squares or SVD (singular value decomposition).

Assume two sets of points: the set in the Bluetooth AOA coordinate system $P_{aoa} = \left\{p_1, p_2, \ldots, p_N\right\}$ in the Bluetooth AOA coordinate system, where $p_i = \left\{x_i, y_i, z_i\right\}^T$, and the point set $P_{vis} = \left\{q_1, q_2, \ldots, q_N\right\}$ where $q_i = \left\{x_i', y_i', z_i'\right\}^T$. The objective is to find the rotation matrix R and translation vector t that minimize the error as defined by Equation (4):

$$\min_{R,t} \sum_{i=1}^{N} \left\| q_i - \left(R p_i + t \right) \right\|^2 \tag{4}$$

First, perform decentralization by calculating the center points of the Bluetooth AOA point set and the visual point set as shown in Equations (5) and (6), respectively, to obtain the decentralized point sets as shown in Equations (7) and (8).

$$\mu_{aoa} = \frac{1}{N} \sum_{i=1}^{N} p_i \tag{5}$$

$$\mu_{vis} = \frac{1}{N} \sum_{i=1}^{N} q_i \tag{6}$$

$$p_i' = p_i - \mu_{aoa} \tag{7}$$

$$q_i' = q_i - \mu_{vis} \tag{8}$$

Then construct the covariance matrix of the decentralized point cloud as shown in Equation (9), where H is a $3x3$ matrix. Next, use SVD to obtain the rotation matrix R as shown in Equations (10) and (11), where U and V in Equation (10) are orthogonal matrices, and Σ is the singular value matrix.

$$H = \sum_{i=1}^{N} p_i' q_i' \tag{9}$$

$$H = U \Sigma V^T \tag{10}$$

$$R = V U^T \tag{11}$$

Finally, calculate the translation vector t as shown in Equation (12).

$$t = \mu_{vis} - R \mu_{aoa} \tag{12}$$

The output data P_{aoa} from the Bluetooth AOA positioning system is transformed into the visual coordinate system via R and t, as shown in Equation (13).

$$P_{vis} = R P_{aoa} + t \tag{13}$$

2.2.2 Coordinate Transformation Based on Hand-Eye Calibration

The principle involves establishing the transformation relationship between the camera coordinate system and the Bluetooth AOA coordinate system through hand-eye calibration. Let the transformation matrix between the camera coordinate system and the Bluetooth AOA coordinate system be given by Equation (14), and the fundamental equation of hand-eye calibration be given by Equation (15), where A in Equation (15) is the camera motion matrix (transformation from the camera coordinate system to the world coordinate system), and B is the motion matrix of the Bluetooth AOA system (transformation from the Bluetooth AOA

coordinate system to the world coordinate system), and X is the transformation matrix between the camera coordinate system and the Bluetooth AOA coordinate system.

$$X = \begin{pmatrix} R & t \\ 0 & 1 \end{pmatrix} \tag{14}$$

$$AX = XB \tag{15}$$

Move the camera and Bluetooth AOA system to record multiple sets of motion data $A_i, B_i (i = 1, 2, \ldots, N)$, each satisfying equation (15). Then decompose the transformation matrix X into a rotation matrix R and a translation matrix t as in equation (14). Extract the rotation components from the motion matrices as in Equation (16), where R_A and R_B represent the rotation components of A and B, respectively. Construct a linear equation system as in Equation (17), express the rotation matrix R as a quaternion or rotation vector, and convert it into a linear equation system for solution.

$$R_A R = R_B R \tag{16}$$

$$R_A R - R_B R = 0 \tag{17}$$

Extract the translation components from the motion matrix as in Equation (18), where t_A and t_B represent the translation components of A and B, respectively. Then construct the linear equation system in Equation (19) and solve it to obtain t. Finally, convert the output data P_{aoa} from the Bluetooth AOA positioning system to the camera coordinate system using Equation (13).

$$R_A t + t_A = R t_B + t \tag{18}$$

$$\left(R_A - I\right) t = R t_B - t_A \tag{19}$$

2.2.3 Feature-Based Coordinate Transformation

The principle involves matching common feature points across two systems to compute the transformation relationship between coordinate systems.

In feature-based coordinate transformation, the RANSAC (Randomized Agreement for Normalized Consistency) algorithm and least squares method are two commonly used approaches for calculating the rotation matrix R and translation vector t, where the least squares method has already been discussed in calibration-based coordinate transformation methods.

RANSAC is a robust estimation algorithm capable of effectively handling outliers in data. Its specific operation consists of the following five steps:

(1) First, randomly sample M points (typically $M = 3$) from the matched point set and use the least squares method to compute the rotation matrix R and translation matrix t.

(2) For all matched points, calculate the transformed error as in Equation (20). Then determine inliers based on the threshold τ: if $\epsilon_i < \tau$, point i is an inlier.

$$\epsilon_i = \left\| q_i - \left(R p_i + t\right) \right\| \tag{20}$$

(3) Step 3: Update the optimal model. If the current number of interior points exceeds the optimal interior point count, update the optimal model (R and t) and record the optimal interior point set.

(4) Step 4: Iterate. Repeat steps (1) to (3) until the maximum iteration count is reached or the interior point ratio meets the requirement.

(5) Step 5: Re-estimate the model. Using the optimal interior point set, recalculate the rotation matrix R and translation matrix t.

After computing R and t, transform the output data P_{aoa} from the Bluetooth AOA positioning system to the visual coordinate system as shown in Equation (13).

2.2.4 Unified Method Based on the World Coordinate System

The principle involves unifying the output data from two systems under a world coordinate system. The operational process is as follows:

First, convert the output data P_{aoa} from the Bluetooth AOA positioning system to the world coordinate system. The world coordinate system is a fixed reference frame, typically the global coordinate system. The AOA coordinate system is a local coordinate system based on the AOA measurement device.

Let the transformation matrix T convert the point P_{AOA} in the AOA coordinate system to the point P_{world} in the world coordinate system, as shown in Equation (21). Here, T is usually composed of a rotation matrix R and a translation matrix t, as described in Equation (22).

$$P_{world} = T \cdot P_{AOA} \tag{21}$$

$$T = \begin{pmatrix} R & t \\ 0 & 1 \end{pmatrix} \tag{22}$$

The rotation matrix R is determined by the rotation angles of the AOA coordinate system relative to the world coordinate system. Assuming the rotation order is ZYX, we have equation (23), where γ, β, α represent the rotation angles about the $\mathrm{Z}, \mathrm{Y}, \mathrm{X}$ axes, respectively. The translation vector t represents the position of the AOA coordinate system origin within the world coordinate system, as given by Equation (24).

$$R = R_z(\gamma) R_y(\beta) R_x(\alpha) \tag{23}$$

$$t = \left[t_x, t_y, t_z \right]^T \tag{24}$$

Then, the output data P_{vis} from the visual localization system is transformed into the world coordinate system as shown in Equation (25). The visual coordinate system is a coordinate system with the camera as its origin. Methods for solving R_{vis} and t_{vis} are typically based on calibration experiments, utilizing known world coordinate system points and their corresponding visual coordinate system points.

$$P_{world} = R_{vis} P_{vis} + t_{vis} \tag{25}$$

Suppose that multiple calibrated points (e.g., checkerboard grids or marker points) of known

position are placed in the world coordinate system, their world coordinates $P_{world}^{i}(i=1,2,\ldots,N)$ are recorded, and a vision system (e.g., a camera) is used to detect these points and record their coordinates P_{vis}^{i} in the visual coordinate system such that Eq. (26) error is minimized to find R_{vis} and t_{vis}.

Then the least squares method is used to find R_{vis} and t_{vis}.

$$P_{world} = R_{vis}P_{vis} + t_{vis} \tag{26}$$

3 Direction estimation for wireless localization based on parallel coordinate descent

The DOA estimation technique realizes high-precision estimation of the incidence direction of the wireless signal source by using the signals received from different spatial bits of communication and combining the phase delay information of the wireless signal arriving at each channel. To address the problem of low estimation accuracy under low signal-to-noise ratio, small snapshot, and multiple sources, the idea of parallel coordinate descent algorithm is borrowed in this chapter to reconstruct the sparse signals and obtain the sparse coefficient matrix of the signals, so as to improve the accuracy of DOA estimation as well as the convergence.

3.1 DOA estimation model based on compressed sensing

The method of transforming the DOA estimation problem into a sparse signal reconstruction problem is to generate a spatial grid by uniformly sampling within the DOA space, where each grid point represents a potential incoming wave direction. Assume that the grid generated by uniform sampling within $[0°,180°]$ is $\boldsymbol{\theta}=\left(\tilde{\theta}_1,\tilde{\theta}_2,\cdots,\tilde{\theta}_N\right), N>M$, where N denotes the number of grids, M denotes the number of array elements, and $r=\left|\tilde{\theta}_1-\tilde{\theta}_2\right|$ denotes the grid spacing. When the grid is dense enough it can be assumed that all incoming wave directions fall on the grid points, assuming that each possible position $\tilde{\theta}_i \in \boldsymbol{\theta}$ corresponds to a potential source signal $\tilde{s}_i(t)$, i.e., the azimuthal angle of only the target signal corresponding to the vector hydrophone output has a large magnitude, while all other azimuthal output magnitudes are small or close to zero. Since $N>M \gg K$, i.e., the number of potential sound sources N is much larger than the number of actual sound sources K, the K sparse signal can be obtained as in Eq. (27):

$$\mathbf{S}(t)=\left(\tilde{s}_1(t),\tilde{s}_2(t),\cdots,\tilde{s}_N(t)\right)^{\mathrm{T}} \in \mathbb{C}^{N\times 1} \tag{27}$$

The original array manifold matrix is shown in Eq. (28):

$$\mathbf{A}(\boldsymbol{\theta})=\left(\mathbf{a}\left(\theta_1\right)\otimes\mathbf{u}_1,\mathbf{a}\left(\theta_2\right)\otimes\mathbf{u}_2,\cdots,\mathbf{a}\left(\theta_K\right)\otimes\mathbf{u}_K\right)\in\mathbb{C}^{3M\times K} \tag{28}$$

It is also extended to an overcomplete redundant dictionary as shown in Equation (29):

$$\begin{aligned}\mathbf{A}(\boldsymbol{\theta}) &= \left(\mathbf{a}\left(\tilde{\theta}_1\right)\otimes\tilde{\mathbf{u}}_1, \mathbf{a}\left(\tilde{\theta}_2\right)\otimes\tilde{\mathbf{u}}_2, \cdots, \mathbf{a}\left(\tilde{\theta}_N\right)\otimes\tilde{\mathbf{u}}_N\right) \\ &\in \mathbb{C}^{3M\times N}\left(\tilde{\mathbf{u}}_k = \left(1, \sin\tilde{\theta}_k, \cos\tilde{\theta}_k\right)^{\mathrm{T}}\right)\end{aligned} \tag{29}$$

This is the projection observation matrix. At this point, the DOA estimation model under the compressed sensing problem can be obtained, and the signal model can be expressed as Equation (30):

$$\mathbf{Y} = \mathbf{A}(\boldsymbol{\theta})\mathbf{S} + \mathbf{N} \tag{30}$$

where under L snap condition, $\mathbf{N} = (\mathbf{N}(1), \mathbf{N}(2), \cdots, \mathbf{N}(L)) \in \mathbb{C}^{3M\times L}$ is the noise vector, $\mathbf{Y} = (\mathbf{Y}(1), \mathbf{Y}(2), \cdots, \mathbf{Y}(L)) \in \mathbb{C}^{3M\times L}$ is the array received data, and the corresponding joint K sparse signal is $\mathbf{S} = (\mathbf{S}(1), \mathbf{S}(2), \cdots, \mathbf{S}(L)) \in \mathbb{C}^{N\times L}$, where the $j(j = 1, 2, \cdots, L)$ th column in $\mathbf{S}$ represents the sparse solution obtained from the j th snap, and the angle corresponding to the position of the non-zero element in the column is the incidence angle of the j th snap.

In summary, after obtaining the received signal model of the vector hydrophone, the angle of the incident signal can be estimated by solving Eq. (30). To simplify the equation, let $\|g\|_0$ denote l_0-paradigm (i.e., the number of non-zero elements), $\|g\|_1$ denote l_1-paradigm, and $\|g\|_2$ denote l_2-paradigm in the following.

Since equation (30) is underdetermined and the solution is not unique, it cannot be solved directly. According to the sparse representation theory, in order to obtain the sparsest solution under the given conditions, the problem is transformed into an optimization problem of minimizing the l_0-paradigm number for solution, as in equation (31):

$$\begin{aligned}&\bar{\mathbf{S}} = \arg\min\left\|\mathbf{S}\right\|_0, \\ &s.t. \mathbf{Y} = \mathbf{AS} + \mathbf{N}.\end{aligned} \tag{31}$$

Since the l_0-paradigm optimization problem is an NP-hard problem, i.e., the correctness and optimality of the solution cannot be determined in polynomial time, it is often solved by convex relaxation methods and greedy class reconstruction algorithms. Convex relaxation methods are global optimal class algorithms that transform the minimization l_0-paradigm optimization problem into a minimization l_1-paradigm optimization problem with inequality constraints as in Equation (32):

$$\begin{aligned}&\bar{\mathbf{S}} = \arg\min\left\|\mathbf{S}\right\|_1 \\ &s.t. \left\|\mathbf{Y} - \mathbf{AS}\right\|_2^2 \leqslant \gamma^2\end{aligned} \tag{32}$$

where γ^2 denotes the standard deviation of noise. Solving equation (32) can be transformed into solving an unconstrained optimization problem as shown in equation (33):

$$\bar{\mathbf{S}} = \min_{\mathbf{S}} \left\{ \lambda \left\| \mathbf{S} \right\|_1 + \frac{1}{2} \left\| \mathbf{Y} - \mathbf{AS} \right\|_2^2 \right\} \tag{33}$$

where λ is the regularization factor.

Transforming the minimization of the l_1-norm optimization problem into a generalized linear programming problem requires solving a second-order cone programming problem. This approach aims for accurate reconstruction by sacrificing computational complexity. The high computational complexity makes this method difficult to apply in large-scale signal fast DOA estimation. Currently, solving the l_1-norm minimization problem using MATLAB's CVX toolbox is a common approach. However, due to the relatively slow solving speed of the CVX toolbox, it is unsuitable for practical applications. To address these issues, this paper employs iterative shrinkage algorithms to solve the signal reconstruction problem in compressed sensing DOA estimation models.

3.2 Parallel Coordinate Descent Algorithm

The coordinate descent algorithm begins with a simple coordinate descent method, then integrates such descent steps into a simpler joint step. Consider a function such as Equation (34):

$$f(\mathbf{x}) = \frac{1}{2} \left\| \mathbf{b} - \mathbf{Ax} \right\|_2^2 + \lambda \mathbf{1}^{\mathrm{T}} \rho(\mathbf{x}) \tag{34}$$

where $\rho(x) = |x|^p$, then $\mathbf{1}^{\mathrm{T}} \rho(x) = \|x\|^p$, λ is a real number.

The Coordinate Descent (CD) algorithm updates only one element of $\mathbf{x}$ at a time, leaving all others unchanged. After m sequential operations (iterating over each element $x \in \mathbb{R}^m$), a converged value is guaranteed. It must be shown that each operation is achieved through contraction.

Assume the current solution is $\mathbf{x}_0$. The goal is to update it based on the i th element $\mathbf{x}_0[i]$ of the current value. This yields a one-dimensional function of the form given by Equation (35):

$$g(z) = \frac{1}{2} \left\| \mathbf{b} - \mathbf{A}x_0 - \mathbf{a}_i \left(z - x_0[i] \right) \right\|_2^2 + \lambda \rho(z) \tag{35}$$

Here, the vector $\mathbf{a}_i$ represents the i th column of $\mathbf{A}$. $\mathbf{a}_i \left(\mathbf{z} - \mathbf{x}_0[i] \right)$ eliminates the influence of the original value and incorporates the new value. If we denote $\mathbf{b} = \mathbf{b} - \mathbf{Ax}_0 + \mathbf{x}_0[i]\mathbf{a}_i$, then the function becomes expression (36):

$$
\begin{aligned}
g(z) &= \frac{1}{2}\left\|\mathbf{b}-\mathbf{a}_i z\right\|_2^2 + \lambda\rho(z) = \frac{1}{2}\left\|\mathbf{b}\right\|_2^2 - \mathbf{b}^{\mathrm{T}}\mathbf{a}_i z + \frac{1}{2}\left\|\mathbf{a}_i\right\|_2^2 \cdot z^2 + \lambda\rho(z) \\
&= \left\|\mathbf{a}_i\right\|_2^2 \left(\frac{\left\|\mathbf{b}\right\|_2^2}{2\left\|\mathbf{a}_i\right\|_2^2} - \frac{\mathbf{a}_i^{\mathrm{T}}\mathbf{b}}{\left\|\mathbf{a}_i\right\|_2^2} z + \frac{z^2}{2} + \frac{\lambda}{\left\|\mathbf{a}_i\right\|_2^2}\rho(z) \right) \\
&= \left\|\mathbf{a}_i\right\|_2^2 \left(\frac{1}{2}\left(z - \frac{\mathbf{a}_i^{\mathrm{T}}\mathbf{b}}{\left\|\mathbf{a}_i\right\|_2^2} \right)^2 + \frac{\lambda}{\left\|\mathbf{a}_i\right\|_2^2}\rho(z) \right) + \text{Constant}
\end{aligned}
\tag{36}
$$

Since minimizing $g(z)$ requires considering only terms containing the variable z, removing the constant term and its coefficient from equation (36) yields equation (37):

$$
G(z) = \frac{1}{2}\left\|z - v_0\right\|_2^2 + \frac{\lambda}{c}\rho(z) \tag{37}
$$

where $\mathbf{v}_0 = \dfrac{\mathbf{a_i}^{\mathrm{T}}\mathbf{b}}{\left\|\mathbf{a_i}\right\|_2^2}, c = \left\|\mathbf{a_i}\right\|_2^2$.

For the above optimization problem, the objective function $G(z)$ can be decomposed into m independent, identical one-dimensional optimization problems to simplify the overall optimization task, as shown in Equation (38):

$$
\begin{aligned}
G(z) &= \frac{1}{2}\left\|z - v_0\right\|_2^2 + \frac{\lambda}{c}\rho(z) \\
&= \sum_{k=1}^{m}\left(\frac{1}{2}\left(z[k] - v_0[k]\right)^2 + \frac{\lambda}{c}\rho(z[k]) \right) \\
&= \sum_{k=1}^{m} g\left(z[k], v_0[k]\right)
\end{aligned}
\tag{38}
$$

Here, $z[k]$ and $v_0[k]$ denote the k th element of vectors z and v_0, respectively.

For scalar functions of the form given by equation (39),

$$
g(z,a) = \frac{1}{2}(z-a)^2 + \lambda\rho(z) \tag{39}
$$

When a convex function is chosen for $\rho(z)$, it can be solved to obtain the global minimum point of the scalar objective function $g(z,\mathbf{a})$ as $\hat{z}_{\text{opt}} = S_{\rho,\lambda}(\mathbf{a})$. Here $S_{\rho,\lambda}(\mathbf{a})$ is obtained as a contraction function which maps the input value $\mathbf{a}$ to the desired output $\hat{z}_{opt}$ and maps values near the origin to zero (i.e., $S_{\rho,\lambda}(a) = 0$ when $|a| \leqslant T$), at which point all values outside this distance are contracted, and the threshold T and the contraction function are both functions with respect to ρ and λ, which results in the globally optimal solution of $G(z)$, namely The globally optimal solution for $g(z)$ is found as in equation (40):

$$\hat{\mathbf{z}}_{\text{opt}} = S_{\rho,\lambda/c}\left(\mathbf{v}_0\right) = S_{\rho,\lambda/c}\left(\frac{\mathbf{a}_i^{\mathrm{T}}\mathbf{b}}{\left\|\mathbf{a}_i\right\|_2^2}\right) = S_{\rho,\lambda/c}\left(\frac{1}{\left\|\mathbf{a}_i\right\|_2^2}\mathbf{a}_i^{\mathrm{T}}\left(\mathbf{b}-\mathbf{A}\mathbf{x}_0\right)+\mathbf{x}_0[i]\right) \tag{40}$$

However, the above algorithm is only applicable to low-dimensional problems, the algorithm needs to extract the columns of $\mathbf{A}$ each time, and it can only determine the product between $\mathbf{A}$ and the accompanying array with a relatively high degree of accuracy, which cannot be directly accurate to the matrix $\mathbf{A}$, and it needs to be modified to the above method. Since there are multiple descending directions in the process of minimizing the function and any non-negative combination of them is also a descending direction, the results of m iterations of the above process are combined linearly. Each step deals with one element of the target vector, whose expression is Eq. (41):

$$\begin{aligned}\mathbf{v}_0 &= \sum_{i=1}^{m}\mathbf{e}_i \times S_{\rho,\lambda/\left\|\mathbf{a}_i\right\|_2^2}\left(\frac{1}{\left\|\mathbf{a}_i\right\|_2^2}\mathbf{a}_i^{\mathrm{T}}\left(\mathbf{b}-\mathbf{A}\mathbf{x}_0\right)+\mathbf{x}_0[i]\right) \\ &= \begin{pmatrix} S_{\rho,\lambda/\left\|\mathbf{a}_1\right\|_2^2}\left(\frac{1}{\left\|\mathbf{a}_1\right\|_2^2}\mathbf{a}_1^{\mathrm{T}}\left(\mathbf{b}-\mathbf{A}\mathbf{x}_0\right)+\mathbf{x}_0[1]\right) \\ \vdots \\ S_{\rho,\lambda/\left\|\mathbf{a}_i\right\|_2^2}\left(\frac{1}{\left\|\mathbf{a}_i\right\|_2^2}\mathbf{a}_i^{\mathrm{T}}\left(\mathbf{b}-\mathbf{A}\mathbf{x}_0\right)+\mathbf{x}_0[i]\right) \\ \vdots \\ S_{\rho,\lambda/\left\|\mathbf{a}_m\right\|_2^2}\left(\frac{1}{\left\|\mathbf{a}_m\right\|_2^2}\mathbf{a}_m^{\mathrm{T}}\left(\mathbf{b}-\mathbf{A}\mathbf{x}_0\right)+\mathbf{x}_0[m]\right) \end{pmatrix}\end{aligned} \tag{41}$$

where $\mathbf{e}_i$ is the m-dimensional unit vector whose ith element is 1 and all other elements are 0. Equation (41) can be rewritten as (42):

$$\mathbf{v}_0 = S_{\rho,\operatorname{diag}\left(\mathbf{A}^{\mathrm{T}}\mathbf{A}\right)^{-1}\lambda}\left(\operatorname{diag}\left(\mathbf{A}^{\mathrm{T}}\mathbf{A}\right)^{-1}\mathbf{A}^{\mathrm{T}}\left(\mathbf{b}-\mathbf{A}\mathbf{x}_0\right)+\mathbf{x}_0\right) \tag{42}$$

where $\operatorname{diag}\left(\mathbf{A}^{\mathrm{T}}\mathbf{A}\right)$ contains the number of paradigms for each column of the dictionary $\mathbf{A}$.

Although each CD direction is descending, a linear combination of them may not guarantee that the whole is descending, so a linear search is needed to find the best linear combination. That is, the actual iterative algorithm is Eq. (43):

$$\begin{aligned}\mathbf{x}_{k+1} &= \mathbf{x}_k + \mu\left(\mathbf{v}_k - \mathbf{x}_k\right) \\ &= \mathbf{x}_k + \mu\left[S_{\rho,\operatorname{diag}\left(\mathbf{A}^{\mathrm{T}}\mathbf{A}\right)^{-1}\lambda}\left(\operatorname{diag}\left(\mathbf{A}^{\mathrm{T}}\mathbf{A}\right)^{-1}\mathbf{A}^{\mathrm{T}}\left(\mathbf{b}-\mathbf{A}\mathbf{x}_k\right)+\mathbf{x}_k\right)-\mathbf{x}_k\right]\end{aligned} \tag{43}$$

Where μ is chosen as required by the linear search algorithm, i.e., the function needs to be optimized in one dimension as in equation (44):

$$h(\mu)=\frac{1}{2}\left\|\mathbf{b}-\mathbf{A}\left(\mathbf{x}_k+\mu\left(\mathbf{v}_k-\mathbf{x}_k\right)\right)\right\|_2^2+\lambda\mathbf{1}^{\mathrm{T}}\rho\left(\mathbf{x}_k+\mu\left(\mathbf{v}_k-\mathbf{x}_k\right)\right) \tag{44}$$

The above process is called parallel coordinate descent algorithm.

In the following, the PCD algorithm is combined with the DOA estimation model based on compressed sensing. To ensure convergence of the algorithm, $\rho(\mathbf{x})=\|\mathbf{x}\|_1$ is chosen so that equation (45) can be obtained:

$$f(\mathbf{x})=\frac{1}{2}\|\mathbf{b}-\mathbf{A}\mathbf{x}\|_2^2+\lambda\|\mathbf{x}\|_1 \tag{45}$$

From the above derivation the optimal solution to the problem represented by Eq. (45) can be found by replacing the vector $\mathbf{x}$ in Eq. (45) with the corresponding $\mathbf{S}$ matrix, the vector $\mathbf{b}$ with the corresponding $\mathbf{Y}$ matrix, and the matrix $\mathbf{A}$ is replaced with the corresponding $\tilde{\mathbf{A}}$ matrix. With this method, the convex optimization problem in the compression-aware multi-snap DOA estimation model can be solved. In summary, the PCD algorithm can be combined with the compression-aware multi-snap DOA estimation model based on compression for DOA estimation.

4 Coordinate domain model of power line based on IoT wireless localization

This section identifies the filtering technique and classification algorithm in the form of comparative experiments based on the coordinate unification technique and wireless localization direction estimation proposed above. Simulation experiments are set up to evaluate the robustness of the proposed wireless localization direction estimation technique. The RTK technique is integrated to construct the power line coordinate domain model based on IOT wireless positioning.

4.1 Filtering techniques and implementation of classification algorithms

This section centers on the performance validation of the localization technique proposed above, testing the localization results under a total of four filtering conditions, namely (W4) no filtering, (W3) mean filtering, (W2) Kalman filtering and (W1) particle filtering.

The CDF performances of this paper's localization technique under different filters for the actual localization of 3, 4 and 5 BLE beacons are shown in Fig. 4(a)-(c) in turn, with the X-axis coordinates being the distance between the localization results and the actual results, and the Z-axis coordinates being the probability. When the number of BLE beacons is 3, the (W1) particle filter shows better performance than the three filters, and 80.00% of its test results are within 2.36m error. And when 4/5 BLE beacons are used for localization, the CDF curves of all 3 filters are closer to each other at 80.00% values of 2.50m and 2.17m, respectively.

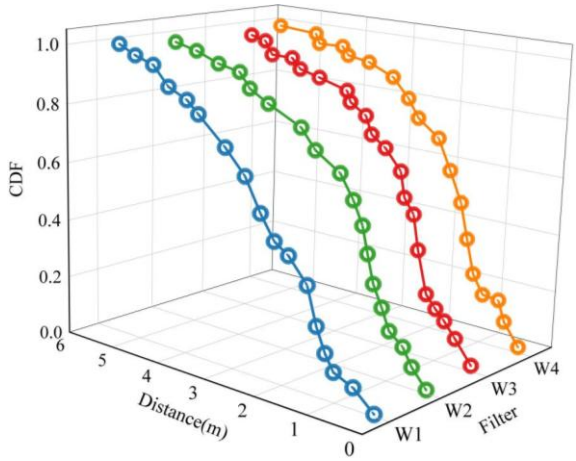

(a) Three BLE beacons

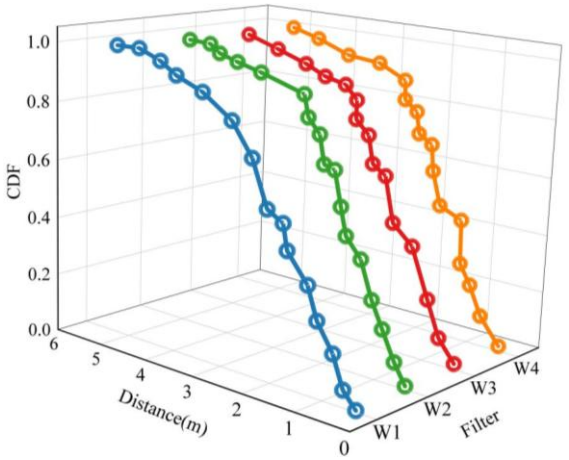

(b) Four BLE beacons

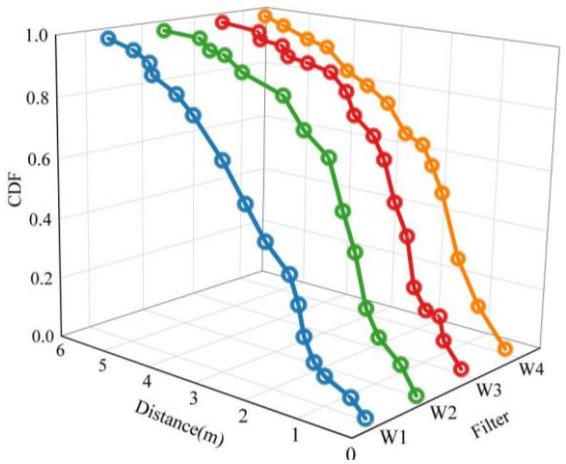

(c) Five BLE beacons

Figure 4: Error CDF curves of different filters

Figures 5(a)-(b) demonstrate the error CDF curves of the particle filter and Kalman filter when the number of BLE beacons for localization varies, and it can be seen that the localization performance of both filters is improved to different degrees as the number of BLE beacons used increases. It originates from the fact that when the number of BLE beacons is increased, the recognition of each RP point is subsequently improved, which makes it easier to match to the nearest point location and improve the accuracy.

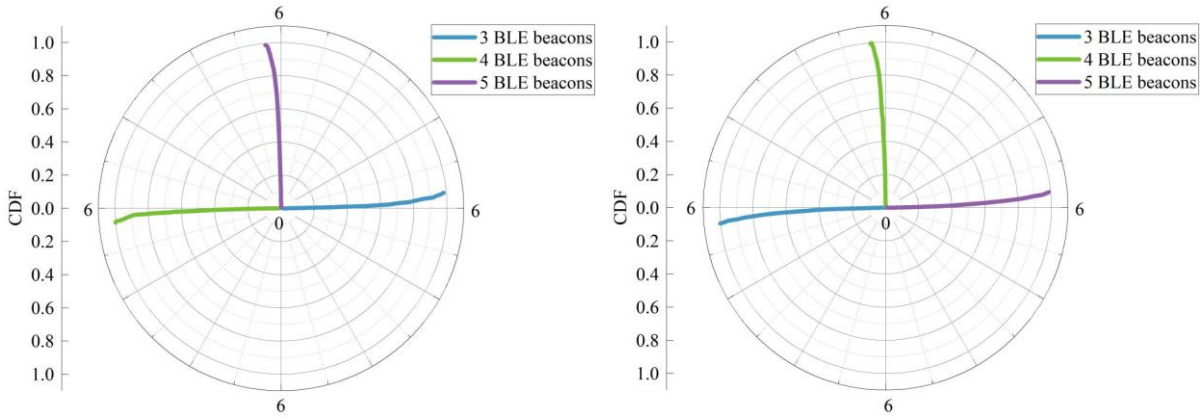

(a) (W1) Particle filter (b) (W2) Kalman filter

Figure 5: Error CDF curves of different BLE beacon quantities

The measured results in Figures 4–5 were obtained using the (M1) minimum Euclidean distance matching method. To further analyze the impact of matching algorithms on positioning results, this paper additionally employed the (M2) w-KNN and (M3) Bayes matching algorithms to obtain CDF curves for five BLE beacons under the (W1) particle filter condition, as shown in Figure 6. Both the (M2) w-KNN and (M3) Bayes matching algorithms significantly improve the positioning performance of the filter within a small error margin of 2m. The (M2) w-KNN matching algorithm demonstrates the best performance, as it does not treat any single RP point as the positioning result. Consequently, the positioning results are more diverse and the curve is smoother.

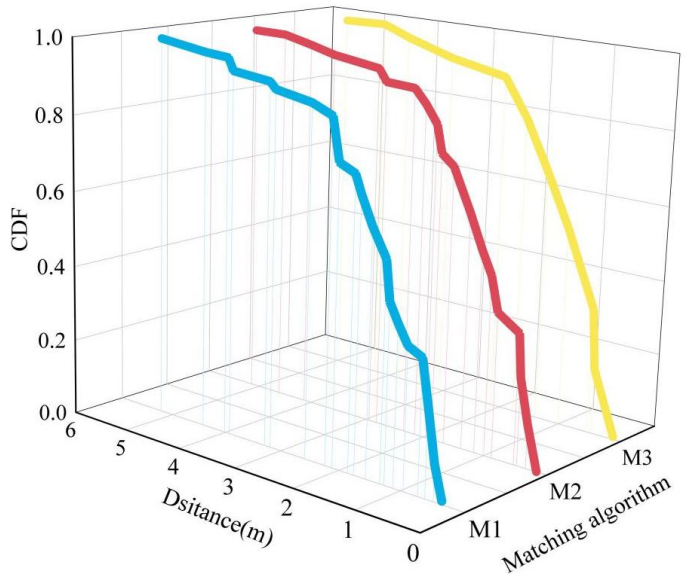

Figure 6: Error CDF curves of different algorithms

Based on the analysis in this section, this paper employs particle filtering technology and the w-KNN matching algorithm to facilitate the subsequent application analysis of the proposed models and techniques.

4.2 Simulation Experiments for Wireless Positioning Direction Estimation

Establish a world coordinate system for the power line tower experiment. The horizontal span is 180 cm, with the power line height at 42.00 cm above ground level at the 90 cm midpoint of the span. The attachment points on both the left and right towers are 63.00 cm above ground level. Based on this, obtain 13 characteristic marker points (numbered 1-13). Based on these 13 markers, three groups were defined: Group A (3, 4, 5, 9, 11, 13), Group B (2, 3, 4, 5, 7, 9, 11, 13), and Group C (1-13). Table 1 presents the calculated results for the mid-span sag of the three groups using the model algorithm in this paper. Depending on the selected reference points, the relative errors in mid-span sag measurements for Groups A, B, and C were 0.951%, 0.459%, and 0.501%, respectively.

Table 1: Measurement results of the central sag group of the gear distance

Group	World coordinate(X,Y)(cm)	Relative error(%)	Sag(cm)
A	(89.9963,42.0055)	0.951	20.9695
B	(90.2342,42.3007)	0.459	20.8126
C	(90.2981,41.9892)	0.501	20.9237

Since Groups B and C selected a larger number of marker points, their relative measurement errors were significantly smaller than those of Group A. However, although Group C had more marker points than Group B, its error remained greater than Group B's. This suggests that the algorithm's error may not be influenced by the number of marker points but instead fluctuates within a fixed range. To test this hypothesis, the Y-values at world coordinates X=30cm, 60cm, 90cm, 120cm, and 150cm were calculated from the coordinate sequences of power lines in Groups A, B, and C. These values were then compared with the measured values h at the corresponding positions of the power lines. The comparison between the extracted calculated results and the measured values h, along with the relative error results, is shown in Table 2. A graphical comparison of the calculated results and the measured values h is presented in Figure 7.

Table 2: The extracted calculation results and relative errors

X		30	60	90	120	150
h		53.1	50.2	48.5	48	48.8
Group A	Y	52.6356	49.8565	48.2069	47.7894	48.7985
	Relative error	0.87	0.68	0.60	0.44	0.00
Group B	Y	52.4582	49.7181	48.3506	48.0074	48.9097
	Relative error	1.21	0.96	0.31	0.02	0.22
Group C	Y	52.5699	49.8948	48.3095	47.8954	48.7861
	Relative error	1.00	0.61	0.39	0.22	0.03

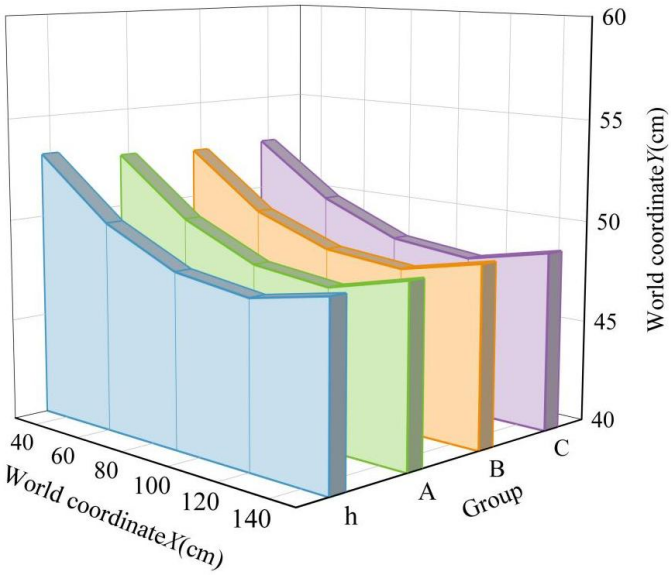

Figure 7: The comparison between the calculation results and the measured values

Combining Table 2 and Figure 7, the model algorithm in this paper produces different results when using different combinations of marked points. Furthermore, when incorporating data from more marked points into the calculations, the overall measurement error exhibited by the model algorithm does not show a significant reduction. However, it can control the relative error within the range of [0.00, 1.00]%. Moreover, the proposed model algorithm consistently produces power line shapes and positions highly similar to actual power lines across different marker point combinations, demonstrating strong computational stability.

4.3 Verification of Positioning Accuracy Based on RTK Technology

Using RTK technology to survey power lines, a 100km-long power line was randomly selected as the experimental subject, containing: 30 corner stakes, 250 straight stakes, and 10 reference stakes. The RTK positioning accuracy statistics under the model algorithm in this paper are shown in Table 3. Overall, both the horizontal and vertical positioning accuracy of target points improved with increasing number of poles, reaching maximum values of 35.89% and 62.19%, respectively. In the straight-line deviation test, the percentage of straight-line alignment reached 85.27% when 200 poles were used.

Table 3: Precision statistics and inspection

Planar point position accuracy	Point position accuracy classification S(m)	S≤0.01	0.01<S ≤0.02	0.02<S ≤0.03	S>0.03
	Number of piles	100	150	35	15
	Proportion	35.89%	49.02%	13.00%	12.45%
Elevation point position accuracy	Point position accuracy classification S(m)	S≤0.02	0.02<S ≤0.03	0.03<S ≤0.04	S>0.04
	Number of piles	180	90	35	10
	Proportion	62.19%	23.56%	11.78%	3.50%
Linear test statistics	Deviation from the straight-line distance S(cm)	|S|<1	1≤|S|<2	2≤|S|<3	|S|>3
	Number of piles	200	45	15	5
	Proportion	85.27%	12.54%	2.68%	0.91%

5 Conclusion

This paper employs coordinate unification technology to enhance DOA estimation accuracy by incorporating a distance metric function into the compressed sensing theory solution process. Through vector contraction and linearization during iteration, the algorithm's computational efficiency is improved, establishing a parallel coordinate descent-based wireless positioning direction estimation method. Simultaneously, particle filtering technology is employed to enhance positioning accuracy. The w-KNN matching algorithm calculates positioning results, and combined with RTK technology, a coordinate domain model for power lines is constructed.

The proposed wireless positioning direction estimation method demonstrates high computational performance and superior operational efficiency in simulation experiments. Its controlled relative error ranges between [0.00, 1.00]%, and it maintains computation results similar to actual values for marked points under different conditions. Supported by RTK technology, the proposed power line coordinate domain model achieves maximum measurement accuracies of 35.89% for planar coordinates and 62.19% for elevation of target points.

About the Authors

Junjie Sun (1997-05), male, Han Nationality, born in Changxing, Zhejiang Province. Master's degree, assistant engineer, research direction is image processing.

Xiang Yuan (1982-10), male, Han Nationality, Taizhou Linhai. Master's degree, associate senior engineer, research interests artificial intelligence technology, data mining.

Keji Chen (1987-05), male, Han Nationality, Ningbo, Zhejiang Province. Master degree, associate senior engineer, research direction: power grid construction project design consultation and disaster prevention and mitigation research.

Bing Wu (1989-08), female, Han Nationality, Hangzhou, Zhejiang province, he is a master's student and senior engineer. His research direction is digital power grid.

Jiarui Yang (1992-06), female, Han Nationality, Qionglai, Sichuan Province. Master's degree, engineer, research direction is infrastructure technology management and power transmission and transformation engineering design technology.

Chutian Yu (1993-09), female, Han Nationality, Shengzhou, Zhejiang Province. Master's degree, engineer, research interests include intelligent power grid and artificial intelligence.

References

[1] Silva Ortega, J. I., Cardenas Escorcia, Y. D. C., & Valencia Ochoa, G. E. (2018). Monitoring electromagnetic fields and safe operation levels in electrical power transmission lines. Chemical engineering transactions, 67.

[2] Wang, J., Chen, J., Xiong, X., Lu, X., Liao, Z., & Chen, X. (2019). Temperature safety analysis and backup protection scheme improvement for overhead transmission line in power oscillation condition. Electric power systems research, 166, 88-98.

[3] Porsius, J. T., Claassen, L., Woudenberg, F., Smid, T., & Timmermans, D. R. (2017). “These Power Lines Make Me Ill”: A Typology of Residents’ Health Responses to a New High-Voltage Power Line. Risk Analysis, 37(12), 2276-2288.

[4] Seong, M., Kim, D. H., & Kim, S. C. (2021). Analysis of electric and magnetic fields distribution and safe work zone of 154 kV power line in underground power cable tunnel. Safety science, 133, 105020.

[5] Hashim, R., Usman, F., & Baharuddin, I. N. Z. (2019). Determining health index of transmission line asset using condition-based method. Resources, 8(2), 80.

[6] Martinez, C., Sampedro, C., Chauhan, A., Collumeau, J. F., & Campoy, P. (2018). The Power Line Inspection Software (PoLIS): A versatile system for automating power line inspection. Engineering applications of artificial intelligence, 71, 293-314.

[7] Zhang, Y., Yuan, X., Li, W., & Chen, S. (2017). Automatic power line inspection using UAV images. Remote Sensing, 9(8), 824.

[8] Sumagayan, M. U., Premachandra, C., Mangorsi, R. B., Salaan, C. J., Premachandra, H. W. H., & Kawanaka, H. (2021). Detecting power lines using point instance network for distribution line inspection. IEEE Access, 9, 107998-108008.

[9] Liu, X., Miao, X., Jiang, H., Chen, J., Wu, M., & Chen, Z. (2022). Component detection for power line inspection using a graph-based relation guiding network. IEEE Transactions on Industrial Informatics, 19(9), 9280-9290.

[10] Zhou, G., Yuan, J., Yen, I. L., & Bastani, F. (2016, September). Robust real-time UAV based power line detection and tracking. In 2016 IEEE International Conference on Image Processing (ICIP) (pp. 744-748). IEEE.

[11] Mishra, D. P., & Ray, P. (2018). Fault detection, location and classification of a transmission line. Neural Computing and Applications, 30(5), 1377-1424.

[12] Chen, Y. C., Banerjee, T., Dominguez-Garcia, A. D., & Veeravalli, V. V. (2015). Quickest line outage detection and identification. IEEE Transactions on Power Systems, 31(1), 749-758.

[13] de Almeida Cardoso, R., Cury, A., & Barbosa, F. (2019). Automated real-time damage detection strategy using raw dynamic measurements. Engineering Structures, 196, 109364.

[14] Sheng, H., & Wang, X. (2019). Online measurement-based estimation of dynamic system state matrix in ambient conditions. IEEE Transactions on Smart Grid, 11(1), 95-105.

[15] Figueiredo e Silva, P., Kaseva, V., & Lohan, E. S. (2018). Wireless positioning in IoT: A look at current and future trends. Sensors, 18(8), 2470.

[16] Bi, S., Cui, J., Ni, W., Jiang, Y., Yu, S., & Wang, X. (2022). Three-dimensional cooperative positioning for Internet of Things provenance. IEEE Internet of Things Journal, 9(20), 19945-19958.

[17] Song, F., Zhu, M., Zhou, Y., You, I., & Zhang, H. (2019). Smart collaborative tracking for ubiquitous power IoT in edge-cloud interplay domain. IEEE Internet of Things Journal, 7(7), 6046-6055.

[18] Saleem, Y., Crespi, N., Rehmani, M. H., & Copeland, R. (2019). Internet of things-aided smart grid: technologies, architectures, applications, prototypes, and future research directions. Ieee Access, 7, 62962-63003.